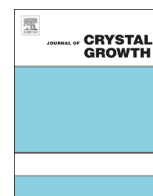




ELSEVIER

Contents lists available at ScienceDirect

Journal of Crystal Growth

journal homepage: www.elsevier.com/locate/jcrysgr

Two-dimensional phase-field study of competitive grain growth during directional solidification of polycrystalline binary alloy

Tomohiro Takaki^{a,*}, Munekazu Ohno^b, Yasushi Shibuta^c, Shinji Sakane^d, Takashi Shimokawabe^e, Takayuki Aoki^e

^a Faculty of Mechanical Engineering, Kyoto Institute of Technology, Matsugasaki, Sakyo-ku, Kyoto 606-8585, Japan

^b Division of Materials Science and Engineering, Faculty of Engineering, Hokkaido University, Kita 13 Nishi 8, Kita-ku, Sapporo, Hokkaido 060-8628, Japan

^c Department of Materials Engineering, The University of Tokyo, 7-3-1 Hongo, Bunkyo-ku, Tokyo 113-8656, Japan

^d Graduate School of Science and Technology, Kyoto Institute of Technology, Matsugasaki, Sakyo-ku, Kyoto 606-8585, Japan

^e Global Scientific Information and Computing Center, Tokyo Institute of Technology, 2-12-1 i7-3 O-okayama, Meguro-ku, Tokyo 152-8550, Japan

ARTICLE INFO

Article history:

Received 28 September 2015

Received in revised form

26 January 2016

Accepted 29 January 2016

Communicated by: M. Plapp

Available online 10 February 2016

Keywords:

A1. Computer simulation

A1. Dendrites

A1. Directional solidification

A1. Crystal morphology

ABSTRACT

Selections of growing crystals during directional solidification of a polycrystalline binary alloy were numerically investigated using two-dimensional phase-field simulations. To accelerate the simulations, parallel graphics processing unit (GPU) simulations were performed using the GPU-rich supercomputer TSUBAME2.5 at the Tokyo Institute of Technology. Twenty simulations with a combination of five sets of different seed orientation distributions and four different temperature gradients covering dendritic and cellular growth regions were performed. The unusual grain selection phenomenon, in which the unfavorably oriented grains preferentially grow instead of the favorably oriented grains, was observed frequently. The unusual selection was more remarkable in the cellular structure than in the dendritic structure.

© 2016 Elsevier B.V. All rights reserved.

1. Introduction

In casting, solidification is usually initiated from the chilled mold surface. A fine equiaxed structure is first formed on the mold surface, followed by the development of a columnar structure [1–3]. Controlling and understanding the growth of the columnar structure is very important because size, morphology, and crystallographic orientations of the columnar structure have a great influence on the ingot surface quality. The columnar structure is formed from grains composed of multiple dendrites or cells. The grain selection was modeled by Walton and Chalmers [4]: the grains with a small angle between the $\langle 100 \rangle$ direction in the cubic metal and the heat flow direction keep growing, while the grains with a large angle grow behind the ones with the small angle, and hence, their growth will be blocked by the ones with the small angle. Fig. 1 schematically illustrates the Walton and Chalmers model [5,6], in which we consider two types of grains: favorably oriented (FO) and unfavorably oriented (UO) along the heat flow direction. Because the growth velocity of UO dendrites, V_{UO} , is higher than that of FO dendrites, V_{FO} , the tip undercooling of the UO dendrite, ΔT_{UO} , is larger than that of FO dendrites, ΔT_{FO} .

* Corresponding author. Tel.: +81 757247317; fax: +81 757247300.
E-mail address: takaki@kit.ac.jp (T. Takaki).

Hence, the UO dendrite tips lag behind the FO dendrite tips [7]. Accordingly, at the converging grain boundary (GB), the FO dendrites block the growth of UO dendrites, and at the diverging GB, the UO dendrites cannot grow along the heat flow direction because of growth suppression by the branching FO dendrites. Consequently, UO grain growth is stopped by the FO grain at both types of GB [8,9]. This model has been widely accepted in studies on the formation of columnar structures.

Recently, an unusual grain selection phenomenon that cannot be explained by the Walton and Chalmers model has been reported in studies on the directional solidification of a bicrystal Ni-based super alloy [10–12]. Specifically, overgrowth of UO grains over FO grains at the converging GB in a bicrystal condition was observed. Hereafter, this overgrowth phenomenon is referred to as “unusual overgrowth,” and “unusual grain selection” is used for the phenomenon where the UO grain overgrows the FO grain regardless of GB type, i.e. converging and diverging. To clarify the unusual overgrowth mechanism, Li et al. performed two-dimensional (2D) phase-field simulations during directional solidification of binary alloy bicrystals [13]. They concluded that the solute interaction around the tips of GB dendrites is a key to the occurrence of the unusual overgrowth. Furthermore, they have confirmed the occurrence of the unusual overgrowth by in-situ observation of a transparent alloy [14]. We also performed detailed and systematic investigations of the unusual overgrowth based on

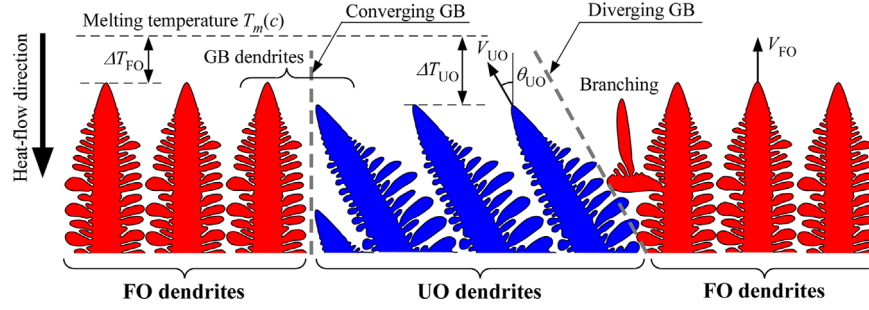


Fig. 1. Dendrite competitive growth model.

large-scale 2D phase-field simulations and reached the following conclusions [15,16]: the unusual overgrowth is a universal phenomenon occurring in metallic materials, the differences in the diffusion layers in front of the FO and UO dendrites at the converging GB had a dominant effect on the unusual overgrowth, and overgrowth occurs when the spacing between the FO dendrite at the GB and the next FO dendrite is approximately equal to a critical minimum spacing. Tourret and Karma also performed a systematic 2D phase-field study on the competitive growth in the bicrystal [17]. It is important to point out that detailed analyses of the unusual overgrowth have been performed only for bicrystal alloys until now. Although the occurrence of the unusual selection was also observed in our recent 3D phase-field simulation of a polycrystal alloy [18], the details of the competitive growth in polycrystal systems such as frequency of the occurrence of the unusual grain selection have not yet been examined.

In this study, in order to investigate the competitive growth phenomena in the 2D polycrystal in detail, we performed systematic phase-field simulations of the polycrystal growth during the directional solidification of a binary alloy. Although the actual competitive growth is a 3D phenomenon, 2D study before the 3D study is essential for the fundamental understanding of the polycrystal competitive growth. Note that this investigation requires significant computational cost even in 2D, because the selections take place over a long time in a large system. To increase the computational speed, we performed a parallel computation using multiple graphics processing units (GPUs) using the supercomputer TSUBAME2.5 at the Tokyo Institute of Technology [16,18–24].

2. Phase-field model and computational conditions

2.1. Quantitative phase-field model

In this study, we simulated the directional solidification of a binary alloy in a 2D system. Here, we extended the quantitative phase-field model for isothermal solidification in a dilute binary alloy developed by Ohno and Matsuura [25] to handle the directional solidification [26] of a polycrystal [18]. The details of the model are discussed in Ref. [15], and here, only the important points are briefly discussed.

The directional solidification in a binary alloy can be described by three variables, temperature T , phase-field ϕ ($\phi = 1$ in solid and $\phi = -1$ in liquid), and nondimensional supersaturation u . The time evolution equations of these variables are given in a 2D system as follows:

$$T(y) = T_0 + G(y - V_p t), \quad (1)$$

$$\tau(\nabla\phi) [1 - (1-k)u] \frac{\partial\phi}{\partial t} = \nabla \cdot [W(\nabla\phi)^2 \nabla\phi] + \frac{\partial}{\partial x} \left[W(\nabla\phi) \frac{\partial W(\nabla\phi)}{\partial\phi_x} \frac{\partial\phi}{\partial y} \right]$$

$$+ \frac{\partial}{\partial y} \left[W(\nabla\phi) \frac{\partial W(\nabla\phi)}{\partial\phi_y} \frac{\partial\phi}{\partial x} \right] - \frac{df(\phi)}{d\phi} - \lambda^* \frac{dg(\phi)}{d\phi} (u + u'), \quad (2)$$

$$\frac{1}{2} [1 + k - (1-k)\phi] \frac{\partial u}{\partial t} = \nabla [D_l q(\phi) \nabla u - j_{AT}] + \frac{1}{2} [1 + (1-k)u] \frac{\partial\phi}{\partial t} - \nabla \cdot J. \quad (3)$$

Here, we employed a frozen temperature approximation, Eq. (1), where T_0 is the reference temperature at $y=0$ and $t=0$, G is the temperature gradient, y is the coordinate along the heat flow direction, V_p is the pulling velocity, and t is the time. u' in Eq. (2) denotes the additional supersaturation for the directional solidification and is defined as $u' = (y - V_p t)/l_T$, where $l_T = \text{Im}(1-k)c_0/(kG)$ is the thermal length, k is the partition coefficient, c_0 is the initial concentration in the liquid, and m is the slope of the liquidus. $\tau(\nabla\phi) = \tau_0 a_s(\nabla\phi)$ and $W(\nabla\phi) = W_0 a_s(\nabla\phi)^2$ are the phase-field relaxation time and interface thickness, respectively, and $a_s(\nabla\phi) = 1 - (3\epsilon_4 + 4\epsilon_4(\phi_x^4 + \phi_y^4))/|\nabla\phi|^4$ represents the crystalline anisotropy with the anisotropic strength ϵ_4 . Here, ϕ_i is the spatial derivative of ϕ with respect to the i direction. We chose $df(\phi)/d\phi = -\phi + \phi^3$ and $dg(\phi)/d\phi = (1 - \phi^2)^2$. λ^* is a coupling constant associated with the thermodynamic driving force and is expressed as $\lambda^* = a_1 W_0/d_0$, where $a_1 = 0.88388$ and d_0 is the chemical capillary length defined by $d_0 = k\Gamma/(\text{Im}(1-k)c_0)$ with the Gibbs–Thomson constant Γ . u is defined as $u = (c_l - c_l^e)/(c_l^e - c_s^e)$, where c_l is the concentration in the liquid, and c_l^e and c_s^e are the equilibrium concentrations in the liquid and solid, respectively, at a temperature T_0 . We followed the Kim–Kim–Suzuki (KKS) model [27] and used the relations $k = c_s^e/c_l^e = c_s/c_l$. Then, the concentration c is given as $c = c_s(1 + \phi)/2 + c_l(1 - \phi)/2$. In Eq. (3), j_{AT} is an antitrapping current expressed as $j_{AT} = -(1 - kD_s/D_l)/(2\sqrt{2})W_0[1 + (1-k)u](\partial\phi/\partial t)\nabla\phi/|\nabla\phi|$ using the diffusion coefficients in the solid, D_s , and liquid, D_l . J is the fluctuating current [26] and $q(\phi)$ is an interpolating function expressed as $q(\phi) = [kD_s + D_l + (kD_s - D_l)\phi]/(2D_l)$.

The polycrystal is expressed using the single phase-field variable introducing the additional parameter expressing the crystal orientation and by performing the coordinate transformation of the gradient of ϕ [15,18]. Eqs. (2) and (3) were discretized based on the standard finite difference method. The moving-frame algorithm was employed to reduce the computational cost.

2.2. Computational conditions

Fig. 2 shows the computational domain and the initial conditions. The computational domain size was set to $L_x \times L_y = 8192\Delta x \times 1536\Delta y = 6.144 \text{ mm} \times 1.152 \text{ mm}$ with a square mesh size of $\Delta x = \Delta y = 0.75 \mu\text{m}$. For both ϕ and u , the periodic boundary condition was set to the left and right ends, and the zero Neumann conditions were applied to the top and bottom ends. The heat flow direction, i.e., the temperature gradient direction, was set to the y -direction. Initially, the computational domain was filled with the liquid Al–3 wt%Cu. Seventeen solid seeds with $3\Delta x$ radius were distributed on the bottom at an interval of $481.9\Delta x$ from the

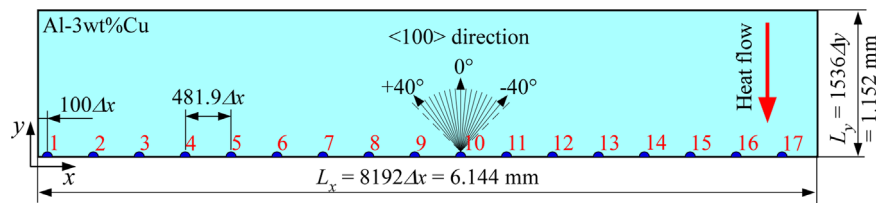


Fig. 2. Computational domain and initial conditions. The red-colored numbers near the bottom indicate the seed number. (For interpretation of the references to color in this figure legend, the reader is referred to the web version of this article.)

Table 1

Crystal orientation θ , which is the counterclockwise angle between the preferred growth $\langle 100 \rangle$ direction and the y -axis, for 17 seeds in 5 sets of simulations (cases 1–5). Unit is degree (deg).

Seed no.	Case 1	Case 2	Case 3	Case 4	Case 5
Seed 1	0.0	-30.3	19.9	19.2	10.9
Seed 2	-35.2	-16.0	-5.4	-29.4	15.2
Seed 3	-30.4	-19.0	29.8	-9.2	-25.2
Seed 4	34.9	34.0	10.4	-24.8	-39.5
Seed 5	-19.9	-10.8	-14.1	40.8	-9.7
Seed 6	-9.7	-35.5	-39.1	4.1	0.0
Seed 7	24.2	5.0	4.9	14.4	-19.5
Seed 8	-14.0	0.0	0.0	9.0	-29.8
Seed 9	29.1	25.8	15.1	-34.7	24.2
Seed 10	-39.6	10.4	24.8	30.6	30.0
Seed 11	9.7	14.7	34.1	0.0	34.4
Seed 12	15.6	20.9	-10.4	-39.5	-34.3
Seed 13	5.8	-25.1	40.8	-4.9	5.4
Seed 14	40.5	30.8	-29.5	-14.1	-4.9
Seed 15	20.2	39.3	-35.6	34.6	20.8
Seed 16	-24.5	-40.6	-19.1	-20.2	-14.2
Seed 17	-4.7	-4.6	-25.3	25.8	40.4

position of $100\Delta x$ from the left end. Each seed has a different preferred growth direction specified by θ , which is an angle counterclockwise to the $\langle 100 \rangle$ direction from the y -axis. θ was varied from -40° to $+40^\circ$ in increments of 5° . Each simulation involves 17 seeds with one for each of these angles. However, these θ have fluctuations between -1° and $+1^\circ$. The seed orientations used in five sets of simulations are shown in Table 1. The seed number in Table 1 corresponds to the red figures in Fig. 2. The simulations are performed for four different temperature gradients $G=10, 30, 90,$ and 270 K/mm under a pulling velocity $V_p=100$ $\mu\text{m/s}$. We selected these different temperature gradients because the primary dendrite arm spacing is proportional to $G^{-0.5}$ [28]. For every temperature gradient, the simulations were performed five times (cases 1–5) with different sets of seed orientations as shown in Table 1. Consequently, twenty simulations were performed. Every computation involved 2×10^7 steps with a time increment Δt . Although the simulations were performed in the 2D system, the computational costs for these large scale and long duration simulations are quite large. Accordingly, we performed the computations with parallel GPUs using eight GPUs in TSUBAME2.5. The actual computational time was within 2 days for each computation. The following data were used in the simulations: $D_l=3 \times 10^{-9}$ m^2/s , $D_s=3 \times 10^{-13}$ m^2/s , $k=0.14$, $\varepsilon_4=0.02$, $\Gamma=0.24 \times 10^{-6}$ Km, $m=-620$ K/at.frac., $c_0=0.013$ at.frac., $T_0=875.7$ K, and $\Delta t=3.75 \times 10^{-5}$ s.

3. Results

As an example, the morphological changes for case 3 every 3.75 s (10^5 steps) until 37.5 s (10^6 steps) and those every 75 s (2×10^6 steps) until 750 s (2×10^7 steps) are shown in Figs. 3 and 4, respectively. The results for the other cases and all movies are

provided in Supplementary materials. The integer numbers on the top of the grains correspond to the orientations θ listed in Table 1. The red-colored numbers in Fig. 3 indicate the grains that are overgrown until the next snapshot. The colors of grains indicate the absolute value of the orientation θ . Snapshots in Figs. 3 and 4 are at an interval of 3.75 s (10^5 steps) and 75 s (2×10^6 steps), respectively, and these correspond to a solidified length of 0.375 mm ($=0.307L_y$) and 7.5 mm ($=6.076L_y$) for a pulling velocity $V_p=100$ $\mu\text{m/s}$. The total solidified length is 75 mm for 750 s (2×10^7 steps). Steady state growth of dendrite tips is achieved until 7.50 s (2×10^5 steps) for all G . Therefore, the conditions at 3.75 s in Fig. 3 are in the region of transient growth. In addition, the detailed orientation relations at the GBs for all twenty computations are given in the tables in Supplementary material.

At 3.75 s for $G=10$ K/mm in Fig. 3, a single dendrite grows from a single seed. The number of primary arms generated at 3.75 s increase as the G increases. When $G=10$ K/mm, the grains with $\theta=-40^\circ$ and -25° are overgrown at 7.5 s. When $G=270$ K/mm, the overgrowth starts at around 18.75 s. Namely, the time at which the overgrowth starts gets delayed with increasing G . In the case of a small G , the dendrites immediately start to grow along the preferred growth direction and the dendritic selection starts immediately, as shown in Fig. 3. On the other hand, in the case of a large G value, the solid seeds first grow along the lateral direction, and then, the flat interface grows along the vertical direction, thus, keeping the interface flat. After that, the interface fluctuates and many primary arms grow. Thus, the time at which the overgrowth starts is delayed in the case of the large G compared to the small G . The moving frame to keep the dendrite tip portions on a constant y -coordinate starts at the 2.4×10^5 th (9 s), 2.2×10^5 th (8.25 s), 2.2×10^5 th (8.25 s), and 2.0×10^5 th (7.5 s) step for $G=10, 30, 90,$ and 270 K/mm, respectively. Therefore, the temperature distributions in the y -direction from 11.25 s onwards in Fig. 3 are different for every G value. The morphologies of the solids are dendritic for $G=10$ and 30 K/mm, cellular for $G=270$ K/mm, and transient between dendritic and cellular shapes for $G=90$ K/mm. At the diverging GBs, branching occurs from one or both grains forming the GB. It can be observed that for $G=10$ and 30 K/mm, the dendrite structures consist of primary, secondary, and tertiary arms and a new primary arm is formed by the tertiary branching. On the other hand, when $G=90$ and 270 K/mm, the growth of a new primary arm originates from a curved secondary arm [17]. In Fig. 3, we can also see that the grains with large θ , such as $\theta=35^\circ$ and -30° , have a tendency to grow quickly and become large in the lateral direction. On the other hand, the grains with small θ , such as $\theta=0^\circ$ and 5° , rarely become large in the lateral direction. In this case, branching is the only option for enlarging grains. Grains with large θ can migrate in the lateral direction and easily become larger when a growth condition where the two neighboring grains grow in directions away from the grain is satisfied.

In the long-duration competitive growth shown in Fig. 4, the grains become larger and the number of grains decreases significantly. The time required to overgrow a grain increases with increasing grain size. Surprisingly, the grains with $\theta=35^\circ$ for $G=10$ and 30 K/mm and with $\theta=-30^\circ$ for $G=270$ K/mm keep

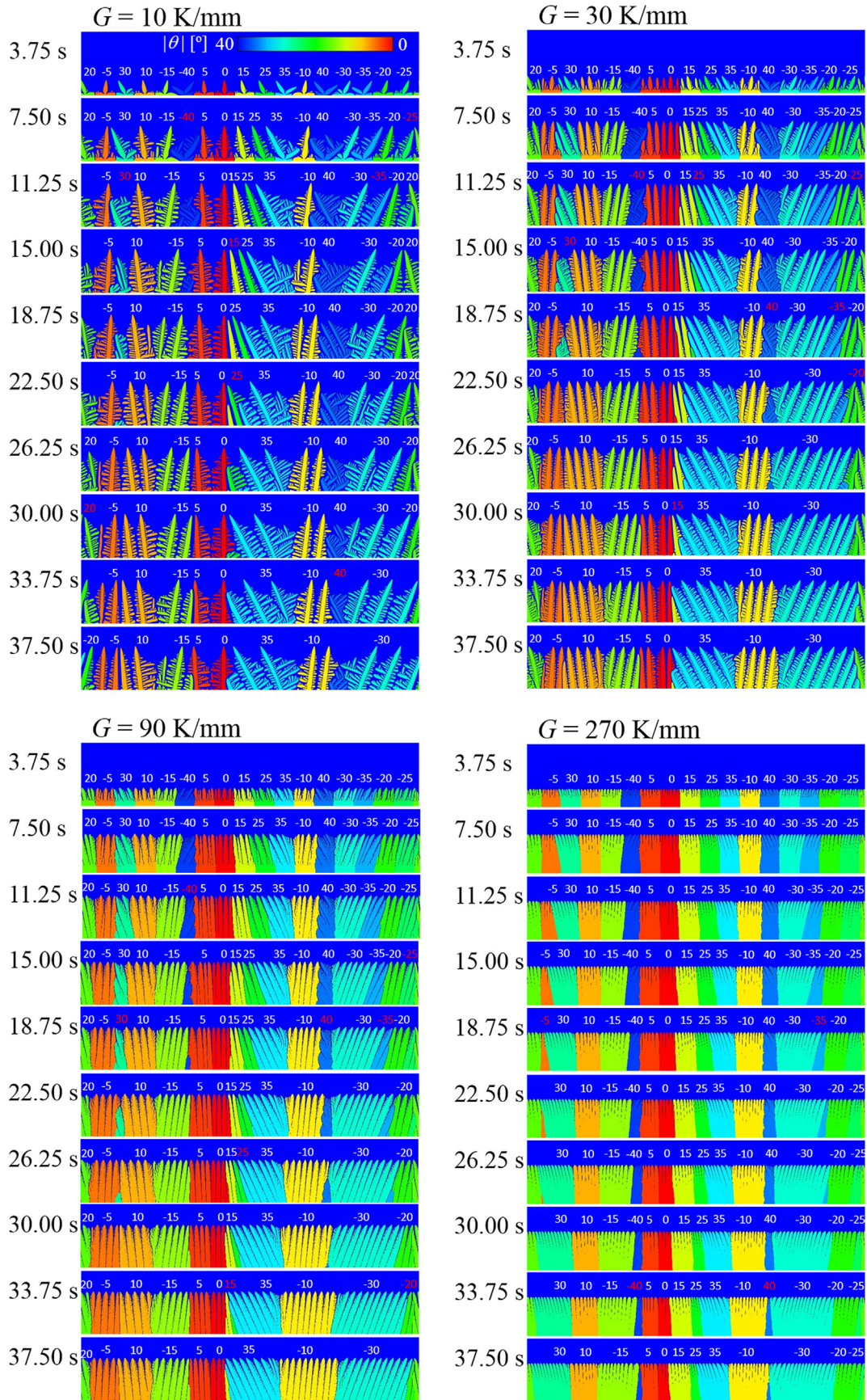


Fig. 3. Snapshots at every 3.75 s (10^5 steps) until 37.5 s (10^6 steps) for case 3. The numbers shown above the grains indicate the crystal orientation θ , and the red-colored numbers show the dendrites that are overgrown until the next snapshot. (For interpretation of the references to color in this figure legend, the reader is referred to the web version of this article.)

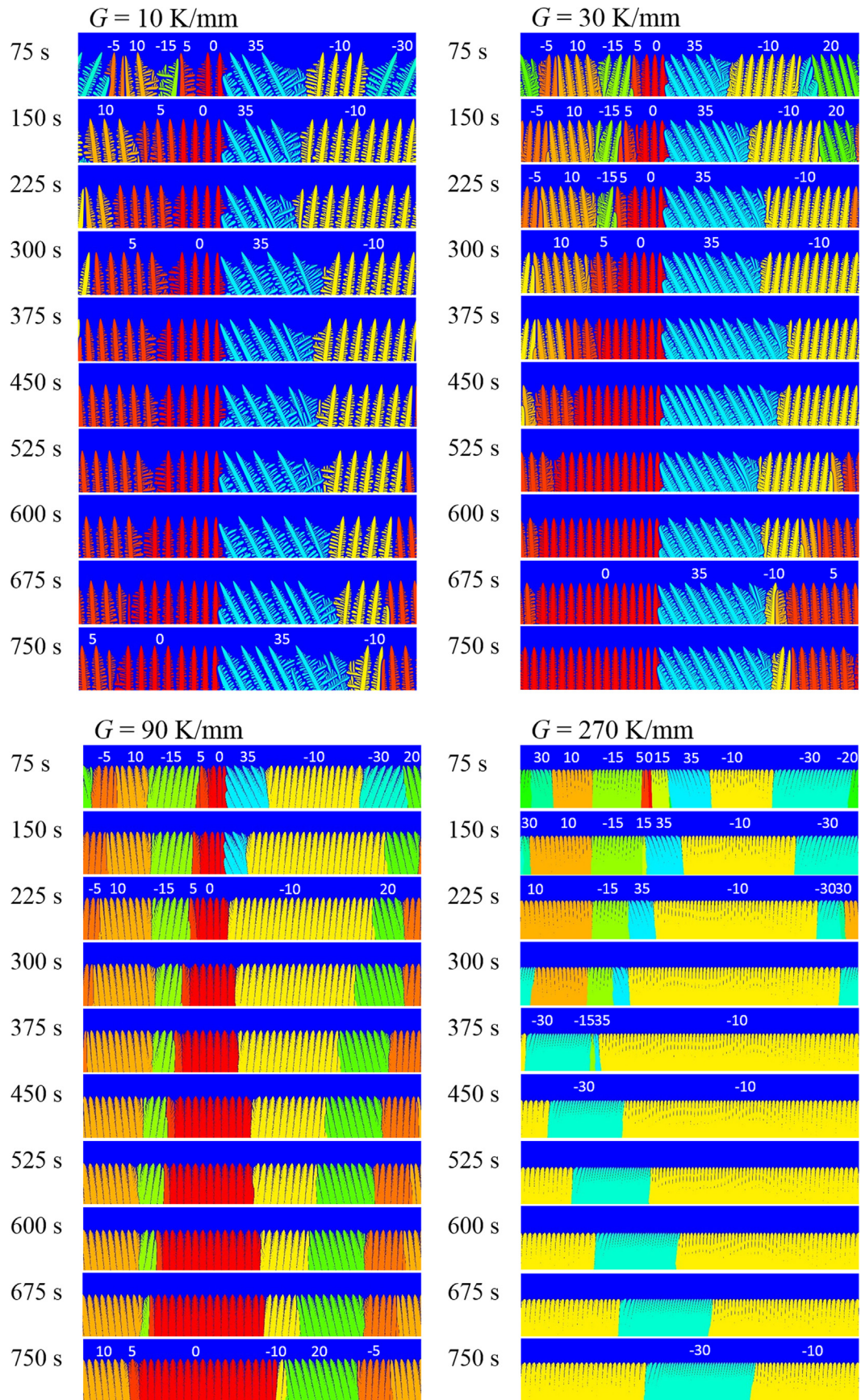


Fig. 4. Snapshots at every 75 s (2×10^6 steps) until 750 s (2×10^7 steps) for case 3. (Movies are available in Supplementary material).

Table 2

The numbers of the dendrites overgrown (negative value) and generated (positive value) at the GBs from 75 s to 750 s for $G=10, 30,$ and 90 K/mm in case 3. The second and bottom rows indicate the number of dendrites surviving at 75 s and 750 s, respectively. The blue (yellow cells) and red (blue cells) fonts indicate the diverging and converging GBs, respectively. Dark blue cells show the converging GB where the unusual overgrowth occurred. The thick solid lines under some cells indicate that the grain is overgrown there.

 $G = 10$ K/mm

Orientation	-5°	10°	5°	0°	35°	-10°	-30°
75 s	1	1	1	2	3	4	3
	0	-1	0				-2
		0	5	1	10	6	0
			-6				6
				-7			-7
750 s			5	8	7	2	

 $G = 30$ K/mm

Orientation	-5°	10°	-15°	5°	0°	35°	-10°	20°
75 s	2	4	3	1	3	4	7	7
	8	-10	-10	13	14	-17	-2	
	0							-5
								-17
								10
								-1
								-37
								-4
750 s				6	16	8	1	

 $G = 90$ K/mm

Orientation	-5°	10°	-15°	5°	0°	35°	-10°	-30°	20°
75 s	3	5	8	1	4	5	15	5	5
	40	-37	-44	48	65	-73	-1		
750 s	6	12		1	19		1		11

growing even at the final step, i.e., 750 s, and the grain with $\theta=0^\circ$ is overgrown after 75 s for $G=270$ K/mm. These phenomena cannot be explained by the conventional competitive growth model shown in Fig. 1. In addition, it can be observed that the position of the diverging GB between grains with $\theta=35^\circ$ and -10° largely fluctuates with time when $G=10$ and 30 K/mm. This is because of the branching competition at the diverging GB. Although such fluctuation is also observed at the diverging GB between $\theta=5^\circ$ and 0° for $G=10$ and 30 K/mm, the extent of the fluctuation of GB is smaller than that of the GB between grains with $\theta=35^\circ$ and -10° , and the GB migrates only to the left side. In the case where the θ of the two grains constituting a diverging GB is large to the plus and minus sides, the GB can migrate to both lateral sides depending on the initiation timing of the tertiary branching. Meanwhile, in the case of small θ on one side of a grain of the diverging GB, the GB migrates to one side but the migration speed also depends on the initiation time of the tertiary branching and is not constant. Furthermore, it can be observed from Fig. 4 that the trajectories of the diverging GB become linear with increasing G ; for example, see the GBs between $\theta=-35^\circ$ and 10° and $\theta=-10^\circ$ and -30° at $G=270$ K/mm in Fig. 4. The converging GBs are relatively straight for all G .

The fact that the unusual overgrowth at the converging GB occurs frequently is clearly shown in Tables A-1–A-20 in Supplementary material. In particular, it is more frequent for the early time stage with a small grain size and for the higher G , especially for $G=270$ K/mm. Table 2 shows the numbers of dendrites that are eliminated (negative value) and are generated by branching (positive value) at the GBs between 75 s and 750 s for $G=10, 30,$ and 90 K/mm in case 3. The same tables for the other cases are shown in Supplementary material. The cell with a solid line frame corresponds to a GB, and, in a cell, there are two numerical figures for the two grains forming the GB, which are separated by one or

two dotted lines in a cell. The blue (yellow background) and red (blue background) figures are for the diverging and converging GBs, respectively. The dark blue cells show the converging GB where the unusual overgrowth occurred. The GB type, i.e. diverging or converging, is determined by the positive and negative of GB misorientation defined by $\Delta\theta=\theta_{left}-\theta_{right}$, where θ_{left} and θ_{right} are the orientation of the grain located at left and right of the GB, respectively; the diverging GB has a positive $\Delta\theta$ and the converging GB has a negative $\Delta\theta$. From Table 2, it is observed that the number of dendrites eliminated and generated at the GBs is larger for large θ . This implies that the overgrowth at the converging GB and the branching at the diverging GB occur more frequently for the grain with large θ . As shown in the dark blue cells, the unusual overgrowth of the FO grain by the UO grain at the converging GB occurs for the FO dendrite with a relatively small number of dendrites. However, even in the case where the unusual overgrowth does not occur, some FO dendrites are eliminated by UO dendrites at the converging GB. In Table 2, at the converging GBs with $\theta=-10^\circ$ and 5° for $G=10$ K/mm, with $\theta=-5^\circ$ and 10° , $\theta=-15^\circ$ and 5° , $\theta=-10^\circ$ and 20° , and $\theta=-10^\circ$ and 20° for 90 K/mm, we can see the overgrowth of some dendrites in the FO grain. In contrast with previous simulations expressing the unusual overgrowth in an ideal bicrystal with one converging GB [15], in the present simulations, the grains have a finite size and two GBs on both sides. Therefore, the unusual overgrowth of the FO grain at the converging GB is not so frequent for the large grains at the later time, but some FO dendrites are eliminated at the converging GB by the UO dendrites.

Fig. 5 shows the changes in the surviving grains for all twenty simulations. The horizontal axis indicates the time and the vertical axis shows the θ of each grain. The right end of the blue bar

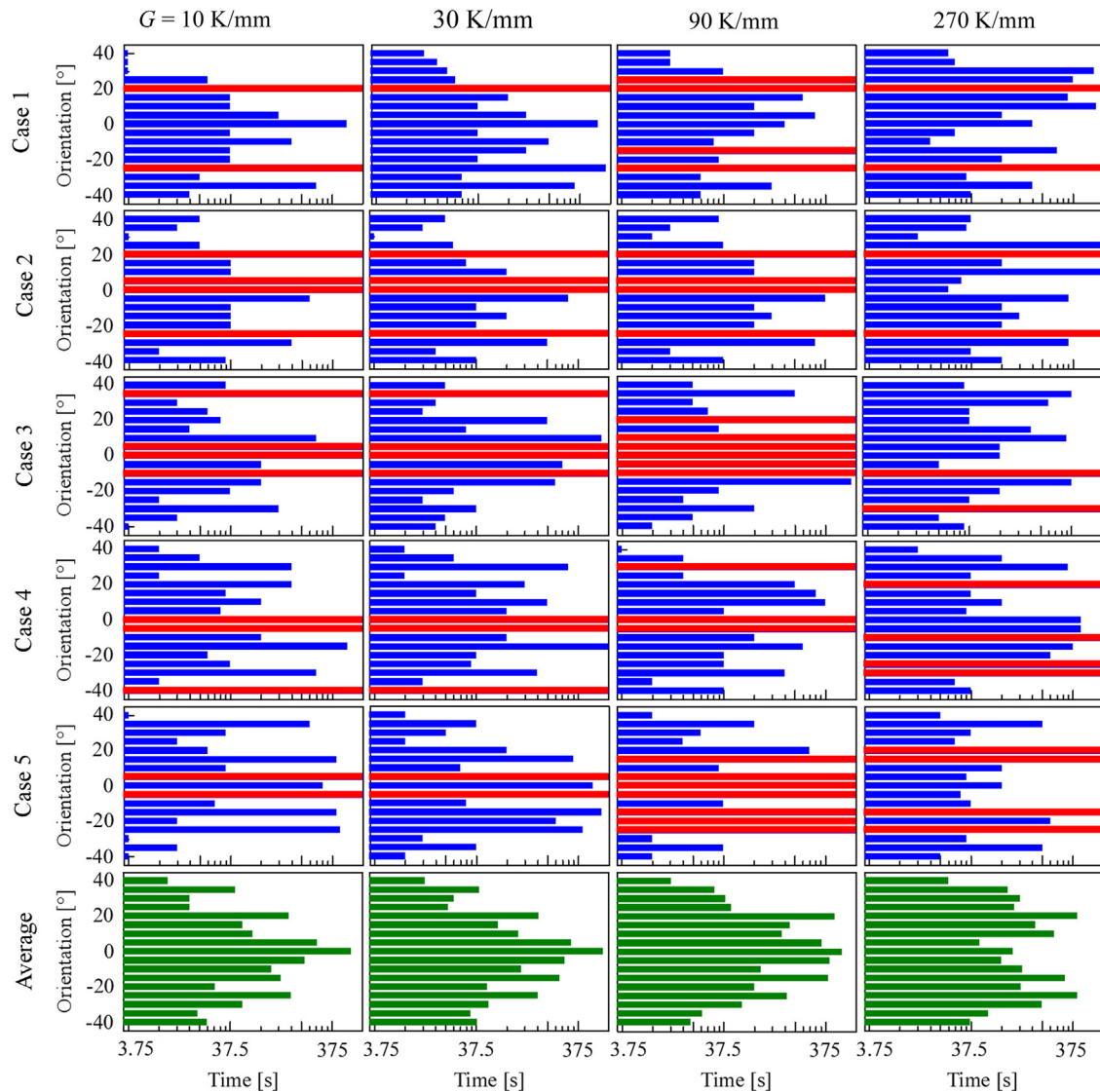


Fig. 5. Changes in the surviving grains for all twenty simulations. The right ends of the bars indicate the point where the grain is overgrown. The grains with the red bar keep growing until end of the simulation. The bottom results with green bars are the average of five cases on the logarithmic scale. (For interpretation of the references to color in this figure legend, the reader is referred to the web version of this article.)

indicates the step number where the grain is overgrown. The grains with the red bar at 750 s keep growing until the end of the present simulation. When $G=10, 30,$ and 90 K/mm, the grains with small θ preferentially grow and the grains with large θ are overgrown in the early stage. This is consistent with the conventional competitive growth model. However, this is not always true. For example, in case 1, only two grains with $\theta=20^\circ$ and -25° , which are relatively large inclinations, finally survive. In cases 1 and 5, the grain with $\theta=0^\circ$ disappears. In cases 3 and 4, the grains with large angles $\theta=35^\circ$ and 40° , respectively, survive until the end of the present simulations. For $G=270$ K/mm, surprisingly, the grains with $|\theta| \leq 5^\circ$ disappear relatively early and cannot keep growing. Many grains with $|\theta| \approx 20^\circ$ survive longer. These selection phenomena cannot be explained by the conventional model and should be categorized as unusual grain selection. The bottom-most results with green bars show the average values of the five cases, which are computed on the logarithmic scale. We can observe a tendency for distribution change where a normal distribution with a single peak for small G gradually changes to a distribution with double peaks as the G increases. This tendency of the change in the grain lifetime distribution depending on the

orientation is interesting. However, we need more systematic studies to obtain an accurate statistical result because the five cases computed for each G are not enough for a statistical evaluation.

Fig. 6 shows the variations in the number of surviving grains and Fig. 7 shows the variations in the number of surviving grains averaged over the five cases for each value of G . In Fig. 6, the number of surviving grains in the five cases for each G value is relatively similar. The starting point of reduction in the number of grains is delayed as G increases, as mentioned above. As can be seen in Fig. 7, the reduction rate is faster for larger G . This implies that the selection between grains occurred more easily in the case of the larger G . In the case of $G=270$ K/mm in Figs. 3 and 4, the grains with $\theta=-5^\circ, 0^\circ, 5^\circ,$ and 10° are easily overgrown by the grains with larger $\theta=30^\circ, 15^\circ, 15^\circ,$ and -30° , respectively. This unusual grain selection (the grain with large θ overgrows the grain with small θ) occurred easily for large G , especially more for the cellular structure than for the dendritic structure. The unusual grain selection accelerates the reduction rate of the number of grains.

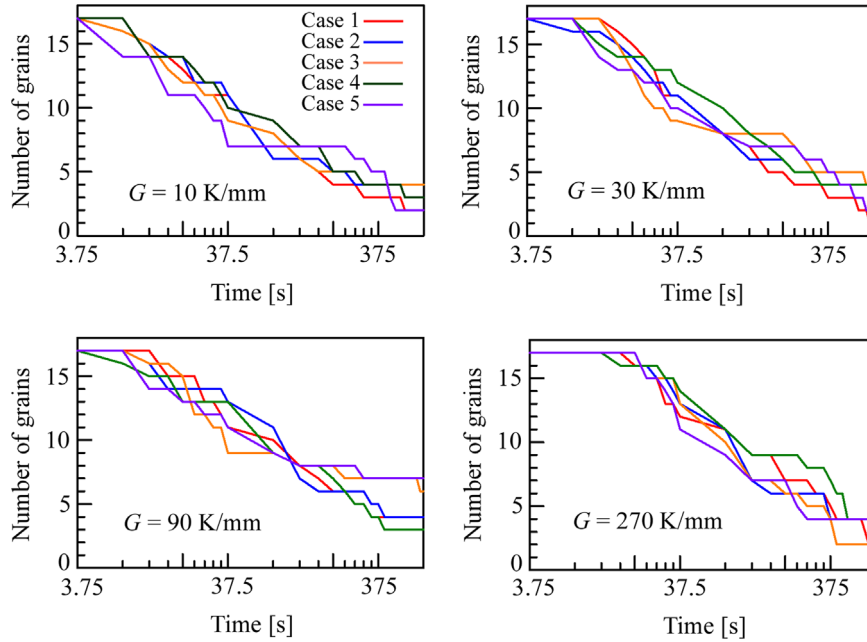


Fig. 6. Changes in the number of the surviving grains.

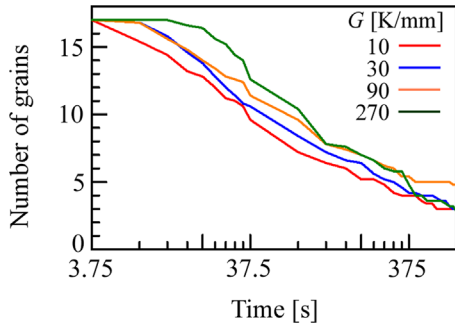


Fig. 7. Changes in the average number of grains for the five computations for every temperature gradient G value.

4. Discussion

The main conclusion of this study is that unusual grain selection, where the unfavorably oriented grains overgrow the favorably oriented ones, occurs frequently in the 2D polycrystal. This cannot be explained by the conventional competitive growth model. Because the present study focuses on the 2D system, the selection between grains is the result of an interaction between two neighboring grains at a GB. Furthermore, because the grain size is finite in a polycrystal, we should consider the migrations of GBs on both sides of a grain. Here, we discuss the situation of the overgrowth of grain A located between two grains B and C in Fig. 8. θ_A , θ_B , and θ_C denote the orientations of the grains A, B, and C. Let us consider three cases: (a) $\theta_B \geq 0$ and $\theta_C \leq 0$, (b) $\theta_B \leq 0$ and $\theta_C \geq 0$, and (c) $\theta_B \leq \theta_A \leq \theta_C$ (all positive or negative).

In the arrangement shown in Fig. 8(a), it was observed that grain A with large $|\theta_A|$ could easily keep growing. The typical example is the grain with $\theta = 35^\circ$ for $G = 10$ and 30 K/mm, shown in Figs. 3 and 4. The arrangement of grains around the grain with $\theta = 35^\circ$ is always identical to the one shown in Fig. 8(a). The grain keeps growing until the end of the simulation and becomes large. The grain with $\theta = -30^\circ$, for all G values shown in Fig. 3, also grows under the arrangement shown in Fig. 8(a). The other examples are shown in Figs. 9 and 10 for case 1 and case 4, respectively, for $G = 30$ K/mm (the detailed morphological changes

are shown in Supplementary material). The grains with $\theta = -35^\circ$, 20° , and -25° in Fig. 9(a), $\theta = -35^\circ$ in Fig. 9(b), $\theta = -30^\circ$, 30° , and -40° in Fig. 10(a), and $\theta = -40^\circ$ in Fig. 10(b, c) are also in the arrangement shown in Fig. 8(a), and the UO grains keep growing for a while and get larger than the other grains. As a result, the grain with a large θ can survive under the arrangement shown in Fig. 8(a). In Fig. 8(a), the converging GB on the left side consists of the grains A and B. At this converging GB, the branching of the dendrite of grain B is suppressed by the growth of the dendrite of grain A, and hence, grain B cannot grow to be large on the right side. The diverging GB on the right side consists of grain A and C. The migration of the right diverging GB is slow in the case of small $|\theta_C|$ and is unstable in the case of large $|\theta_C|$, as observed in Fig. 4. On the other hand, for $G = 90$ and 270 K/mm in Figs. 3 and 4, the grain with $\theta = 35^\circ$ in the arrangement shown in Fig. 8(a) disappeared finally in contrast to the case for $G = 10$ and 30 K/mm. This is due to the monotonic migration of the right diverging GB to the left. This difference is caused by the different branching mechanism [17]. It is also noted that even if grain A in the case of $G = 10$ and 30 K/mm is in the arrangement shown in Fig. 8(a) at a certain moment, it does not necessarily survive until the end, as indicated by the examples of grains with $\theta = -35^\circ$ in Fig. 9 and $\theta = -30^\circ$ and 30° in Fig. 10, because the grain arrangement changes when the neighboring grains disappear.

In the arrangement shown in Fig. 8(b), grain A is relatively easily overgrown by the grains on both sides, even when $|\theta_A|$ is small. The best example is the grain with $\theta = 0^\circ$ shown in Fig. 9(c). The grain with $\theta = 0^\circ$ is overgrown by the grains on both sides with $\theta = -25^\circ$ and 20° . In case 5 for $G = 10$ and 30 K/mm, the grain with $\theta = 0^\circ$ is also overgrown, from the arrangement shown in Fig. 8(b). This is the same phenomenon explained in references [13,15]. This unusual overgrowth will not occur in cases of high V_p and large θ for grains B or C [13,15,17]. In particular, if grain A is small, the grain is overgrown easily, because the arm spacing between the dendrites in grain A easily becomes small when grains B and C approach grain A [15]. Here, the overgrowth of the grain with $\theta = 0^\circ$ for $G = 270$ K/mm shown in Figs. 3 and 4 is not the same as that in Fig. 9(c).

In the arrangement shown in Fig. 8(c), grain A is often overgrown by grain C with larger inclination angles than grain A.

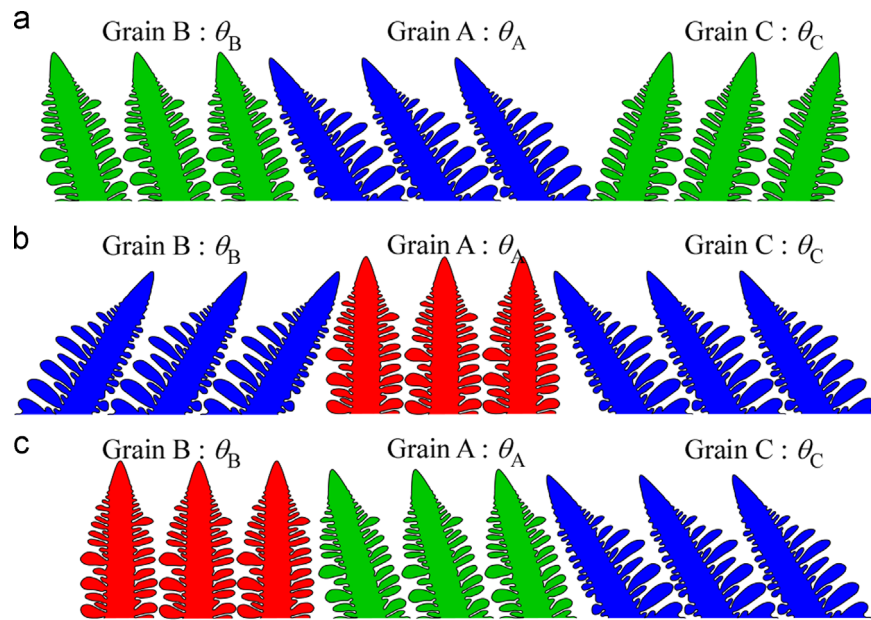


Fig. 8. Orientation relations in three grain systems. (a) $\theta_B \geq 0$ and $\theta_C \leq 0$, (b) $\theta_B \leq 0$ and $\theta_C \geq 0$, and (c) $\theta_B \leq \theta_A \leq \theta_C$.

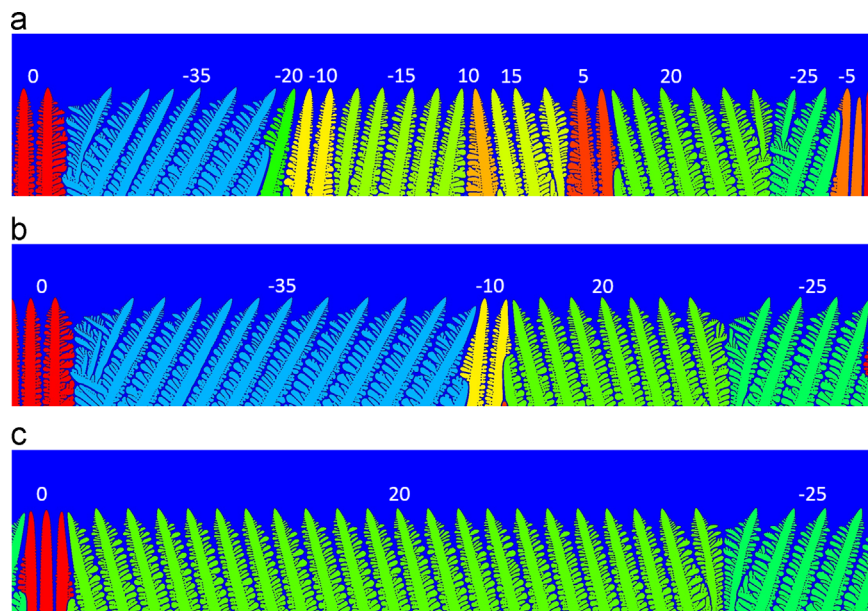


Fig. 9. Snapshots in case 1 for $G=30$ K/mm: (a) 37.5 s (10^6 th step), (b) 150 s (4×10^6 th step), and (c) 525 s (14×10^6 th step).

Examples are shown for the grains with $\theta=15^\circ$, 25° , and -20° in Fig. 3 for $G=10$, 30, and 90 K/mm and the grain with $\theta=-20^\circ$ shown in Fig. 9(a). This unusual overgrowth occurs when the migration rate of the right GB of grain A is faster than that of the left GB.

In the case of the cellular structure for $G=270$ K/mm, the unusual overgrowth occurred much more easily than in the case of the dendritic structures for $G=10$, 30, and 90 K/mm. This is clear from Fig. 5, where many grains with small θ disappear successively. The detailed orientation relations at the converging GBs where the unusual overgrowth occurs are shown in the tables in Supplementary material. In Figs. 3 and 4, the grains with small $\theta=-5^\circ$, 0° , and 5° are overgrown by the grains with larger $\theta=30^\circ$, 15° , and -15° , respectively. At the converging GB shown in Fig. 1, the lateral migration of the FO dendrite is a key to determining whether the unusual overgrowth will occur and for determining

the overgrowth speed [15]. In the case of the dendrite structure, the FO dendrite at the GB can escape to the left when the UO dendrite approaches the FO dendrite. Then, the unusual overgrowth can be delayed. On the other hand, in case of the cellular structure, the escape to the left is difficult, because the arm spacing between the FO dendrites is small. In addition, the interaction period between the GB dendrites is shorter for the cellular structure than the dendritic structure, owing to the small arm spacing. As a result, the unusual overgrowth at the converging GB in the cellular structure occurs much more frequently than in the dendritic structure. At the diverging GB, the branching was generated periodically, whereas the branching timing was more random for the lower G . The periodic branching is thought to form the linear GB trajectories of the diverging GB for the high G . On the other hand, we need further investigations for the different competition at the GB in the dendrite and cell structures.

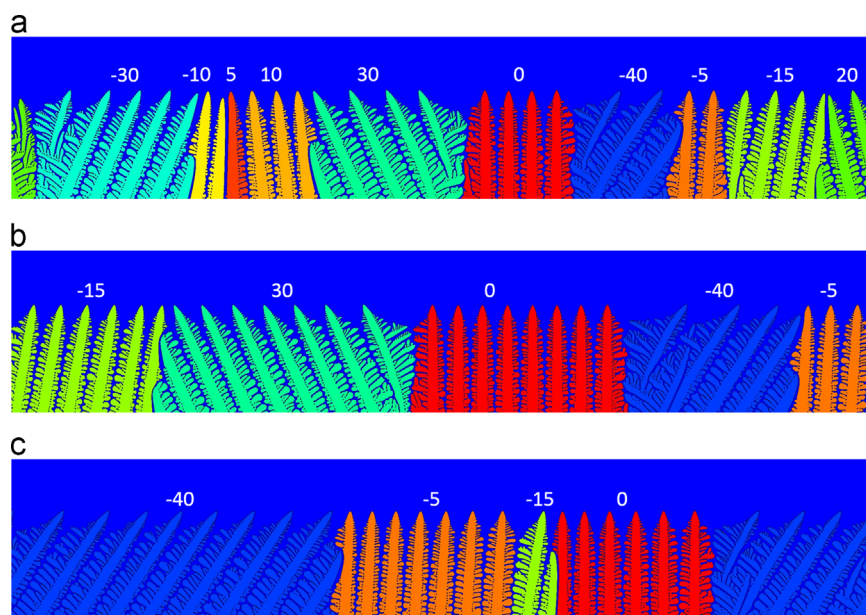


Fig. 10. Snapshots in case 4 for $G=30$ K/mm: (a) 75 s (2×10^6 th step), (b) 225 s (6×10^6 th step), and (c) 750 s (2×10^7 th step).

We can see some grain selection at the transient growth until 7.5 s in Fig. 3. Such grain selections in the transient growth are not similar to those in the steady state growth. Therefore, we need further detailed studies regarding grain competition at the transient growth by considering the effects of the initial undercooling, the initial seed spacing, the nucleation rate, and the nucleation method (cite saturated or continuous). Even in the steady state growth, the effect of the initial transient condition is also important.

5. Conclusions

Dendrite and cell selections during directional solidification of polycrystalline binary alloy were investigated by performing two-dimensional phase-field simulations. Twenty simulations with five different sets of initial seed distributions and four different temperature gradients were performed. Each simulation was performed for 750 s (2×10^7 steps) in a computational domain of $6.144 \text{ mm} \times 1.152 \text{ mm}$ (8192×1536 meshes). Because these are computationally quite expensive even in the 2D simulation, parallel computation was performed using eight GPUs using the supercomputer TSUBAME2.5 at the Tokyo Institute of Technology. The main conclusion of this study is that the unusual grain selection, i.e., the overgrowth of unfavorably oriented grains over favorably oriented ones, is observed frequently. In other words, the inclined dendrites may continue growing if a certain condition is satisfied. The other conclusions are as follows:

- The unfavorably oriented grain easily becomes large under a certain growth condition where the two neighboring grains grow in directions away from the grain, because it grows diagonally. In such dendrite arrangement, the unfavorably oriented grain can survive even with a large inclination angle.
- The favorably oriented grain with a very small inclination angle rarely becomes large although the survival rate is high, because branching is the only option for enlarging the grain. When the favorably oriented grain is in a condition where the neighboring two grains grow toward the grain, the grain is easily overgrown even with very small inclination angle.

- The grain coarsening speed or speed of reduction in the number of grains is higher in the cellular structure than in the dendrite structure. This is because unusual overgrowth at the converging GB occurs more easily for the cellular structure than for the dendrite structure.
- The position of diverging GB largely fluctuates in the dendrite structure and linearly changes in the cell structure. This is due to the different branching mechanisms: in the dendrite structure, the tertiary arm becomes the primary arm, and in the cell structure, the secondary arm directly grows into the new primary arm.

Acknowledgments

This research was supported by ISIJ Research Promotion Grants from the Iron and Steel Institute of Japan (ISIJ), Grant-in-Aid for Scientific Research (B) (Nos. 25289006 and 25289266) from Japan Society for the Promotion of Science (JSPS), Grant-in-Aid for Scientific Research (S) (No. 26220002) from the Ministry of Education, Culture, Sports, Science and Technology (MEXT), Joint Usage/Research Center for Interdisciplinary Large-scale Information Infrastructures (JHPCN) and High Performance Computing Infrastructure (HPCI) in Japan, and the Computational Materials Science Initiative (CMSI). The authors thank the Global Scientific Information and Computing Center, Tokyo Institute of Technology for allowing the use of the TSUBAME 2.5 supercomputer.

Appendix A. Supplementary material

Supplementary data associated with this article can be found in the online version at <http://dx.doi.org/10.1016/j.jcrysgro.2016.01.036>.

References

- [1] W. Kurz, D.J. Fisher, *Fundamentals of Solidification*, Trans Technol Publications Ltd., Switzerland, 1989.
- [2] J.A. Dantzig, M. Rappaz, *Solidification*, EPFL Press, 2009.
- [3] D.M. Stefanescu, *Science and Engineering of Casting Solidification*, second edition, Springer US, New York, 2009.

- [4] D. Walton, B. Chalmers, The origin of the preferred orientation in the columnar zone of ingots, *Trans. Metall. AIME* 215 (1959) 447–457.
- [5] C.A. Gandin, M. Rappaz, A coupled finite element-cellular automaton model for the prediction of dendritic grain structures in solidification processes, *Acta Metall. Mater.* 42 (1994) 2233–2246.
- [6] M. Rappaz, C.A. Gandin, Probabilistic modelling of microstructure formation in solidification processes, *Acta Metall. Mater.* 41 (1993) 345–360.
- [7] W. Kurz, B. Giovanola, R. Trivedi, Theory of microstructural development during rapid solidification, *Acta Metall.* 34 (1986) 823–830.
- [8] H. Esaka, M. Tamura, K. Shinozuka, Analysis of yield rate in single crystal casting process using an engineering simulation model, *Mater. Trans.* 44 (2003) 829–835.
- [9] H. Esaka, K. Fujita, H. Daimon, M. Tamura, K. Shinozuka, Effect of interfacial morphology on grain selection in unidirectional solidification, *J. Jpn. Inst. Met.* 64 (2000) 1206–1211.
- [10] N. D'Souza, M.G. Ardakani, A. Wagner, B.A. Shollock, M. McLean, Morphological aspects of competitive grain growth during directional solidification of a nickel-base superalloy, CMSX4, *J. Mater. Sci.* 37 (2002) 481–487.
- [11] A. Wagner, B.A. Shollock, M. McLean, Grain structure development in directional solidification of nickel-base superalloys, *Mater. Sci. Eng. A* 374 (2004) 270–279.
- [12] Y.Z. Zhou, A. Volek, N.R. Green, Mechanism of competitive grain growth in directional solidification of a nickel-base superalloy, *Acta Mater.* 56 (2008) 2631–2637.
- [13] J. Li, Z. Wang, Y. Wang, J. Wang, Phase-field study of competitive dendritic growth of converging grains during directional solidification, *Acta Mater.* 60 (2012) 1478–1493.
- [14] H. Yu, J. Li, X. Lin, L. Wang, W. Huang, Anomalous overgrowth of converging dendrites during directional solidification, *J. Cryst. Growth* 402 (2014) 210–214.
- [15] T. Takaki, M. Ohno, T. Shimokawabe, T. Aoki, Two-dimensional phase-field simulations of dendrite competitive growth during the directional solidification of a binary alloy bicrystal, *Acta Mater.* 81 (2014) 272–283.
- [16] Y. Shibuta, M. Ohno, T. Takaki, Solidification in a supercomputer: from crystal nuclei to dendrite assemblages, *JOM* 67 (2015) 1793–1804.
- [17] D. Touret, A. Karma, Growth competition of columnar dendritic grains: a phase-field study, *Acta Mater.* 82 (2015) 64–83.
- [18] T. Takaki, T. Shimokawabe, M. Ohno, A. Yamanaka, T. Aoki, Unexpected selection of growing dendrites by very-large-scale phase-field simulation, *J. Cryst. Growth* 382 (2013) 21–25.
- [19] T. Shimokawabe, T. Aoki, T. Takaki, A. Yamanaka, A. Nukada, T. Endo, N. Maruyama, S. Matsuoka, Peta-scale phase-field simulation for dendritic solidification on the TSUBAME 2.0 supercomputer, in: *Proceedings of 2011 SC—International Conference for High Performance Computing, Networking, Storage and Analysis*, 2011.
- [20] A. Yamanaka, T. Aoki, S. Ogawa, T. Takaki, GPU-accelerated phase-field simulation of dendritic solidification in a binary alloy, *J. Cryst. Growth* 318 (2011) 40–45.
- [21] T. Takaki, Phase-field modeling and simulations of dendrite growth, *ISIJ Int.* 54 (2014) 437–444.
- [22] S. Sakane, T. Takaki, M. Ohno, T. Shimokawabe, T. Aoki, GPU-accelerated 3D phase-field simulations of dendrite competitive growth during directional solidification of binary alloy, *IOP Conf. Ser. Mater. Sci. Eng.* 84 (2015) 012063.
- [23] T. Takaki, R. Rojas, M. Ohno, T. Shimokawabe, T. Aoki, GPU phase-field lattice Boltzmann simulations of growth and motion of a binary alloy dendrite, *IOP Conf. Ser. Mater. Sci. Eng.* 84 (2015) 012066.
- [24] Y. Shibuta, K. Oguchi, T. Takaki, M. Ohno, Homogeneous nucleation and microstructure evolution in million-atom molecular dynamics simulation, *Sci. Rep.* 5 (2015) 13534.
- [25] M. Ohno, K. Matsuura, Quantitative phase-field modeling for dilute alloy solidification involving diffusion in the solid, *Phys. Rev. E* 79 (2009) 031603.
- [26] B. Echebarria, A. Karma, S. Gurevich, Onset of sidebranching in directional solidification, *Phys. Rev. E* 81 (2010).
- [27] S.G. Kim, W.T. Kim, T. Suzuki, Phase-field model for binary alloys, *Phys. Rev. E* 60 (1999) 7186–7197.
- [28] M. Gündüz, E. Çadırılı, Directional solidification of aluminium–copper alloys, *Mater. Sci. Eng. A* 327 (2002) 167–185.